

Research Article

Multielement Imaging Reveals the Diagenetic Features and Varied Water Redox Conditions of a Lacustrine Dolomite Nodule

Yuke Liu ^{1,2}, Wenyuan He,³ Jinyou Zhang,³ Zhenwu Liu,^{1,4} Fazi Chen,^{1,4} Huajian Wang ^{1,2}, Yuntao Ye,⁵ Yitong Lyu,^{1,2} Zhiyong Gao,^{1,2} Zhichao Yu,^{1,2} Lina Bi,^{1,2} and Shuichang Zhang^{1,2}

¹Research Institute of Petroleum Exploration and Development, Beijing 100083, China

²Key Laboratory of Petroleum Geochemistry, China National Petroleum Corporation, Beijing 100083, China

³Daqing Oil Field Company, China National Petroleum Corporation, Daqing 163000, China

⁴School of Ocean Sciences, China University of Geosciences, Beijing 100083, China

⁵School of Earth and Space Sciences, Peking University, Beijing 100871, China

Correspondence should be addressed to Huajian Wang; wanghuajian@petrochina.com.cn

Received 21 May 2021; Revised 26 September 2021; Accepted 1 December 2021; Published 10 January 2022

Academic Editor: Chao Liang

Copyright © 2022 Yuke Liu et al. This is an open access article distributed under the Creative Commons Attribution License, which permits unrestricted use, distribution, and reproduction in any medium, provided the original work is properly cited.

The genesis of dolostone has long been puzzling for more than two centuries. Although much work has been done on investigating the process of dolomitization, little emphasis has been put on examining the diagenetic water redox condition with the wealthy geochemical information preserved in primary dolomite, which is believed to archive the aqueous environment as well as biotic and/or abiotic effects during formation. *In situ* interpretation with high resolution is a prerequisite in refined research of dolomite. Here, we reported the multielement imaging results of a lacustrine dolomite nodule with the host black shale from the Songliao Basin, northeast of China. Micro X-ray fluorescence (μ -XRF) with a spatial resolution down to $10\ \mu\text{m}$ was used for in situ scanning. Two key parameter settings of the μ -XRF, including single-point exposure time and spatial resolution, were optimized to achieve a better result in a reasonable scanning time scale. The final imaging data graphically revealed dynamic variation of elemental distributions, including elements enriched in dolomite (e.g., Ca, Mg, Fe, and Mn), clastic quartz (Si), and clay minerals (e.g., Al and K) and redox-sensitive trace elements (e.g., Cr, Mo, V, and U). The well-preserved laminated structures inside the nodule and the features with a magnesium-rich core wrapped with an iron-concentric outer layer and a manganese-concentric shell together indicated its primary form as dolomite and a gradual transformation into ankerite as well as manganese-ankerite. The elemental variation indicates a varied bottom water redox condition, which involved from sulfidic to ferruginous and manganous zones. Here, we propose that the intermittent supplies of sulfate and Fe-/Mn-oxidized minerals interrupting the black shale deposition while favoring dolomitization might be brought by the oxidized and salted seawater. And this lacustrine dolomite is expected to be a potential fingerprint mineral in tracking the seawater intrusions to the Songliao Basin which happened 91 million years ago.

1. Introduction

Ever since the first description of dolomite ($\text{CaMg}(\text{CO}_3)_2$) by Dolomieu [1] more than 200 years ago, the genesis of dolomite deposit has long been puzzling and gives rise to the so-called “dolomite problem” [2]. Being one kind of dolomite, ankerite ($\text{Ca}(\text{Fe}, \text{Mg})(\text{CO}_3)_2$) is formed when more than half of magnesium is replaced by iron. Up to now, understanding the genesis of dolostone has long been

a particularly intriguing challenge [3], as the lack of modern analogues is a major stumbling block in relating the growth of those ancient dolostones to the observations of modern sediments [4].

So far, massive dolostones are attributed to slow burial or hydrothermal dolomitization of calcite or aragonite precursors by Mg-rich fluids at temperatures of $>100^\circ\text{C}$ [3, 5, 6]. In contrast, other studies have asserted that dolomites can form at low temperatures in pore waters during early

diagenesis [7, 8]. According to the theory of penecontemporaneous replacement, early diagenetic dolomitization of calcite or aragonite precursors occurred at temperatures of $<60^{\circ}\text{C}$ via Mg-rich reflux in pore water [9]. With the evidence of evaporitic mineral remnants, penecontemporaneous replacement has been consolidated as the Triassic Dolomia Principale of the Dolomite Mountains of Italy, shallow-marine dolostone units, and some saline lacustrine dolomite deposit under strong evaporation [10, 11]. Another mechanism advocating the primary genesis is the organogenic or bacteria-induced dolomite model. This one primarily involves direct precipitation of high-Mg calcite and dolomite from water or pore water in near-surface sediment under microbial-organic mediation [12], followed by the transformation to a more ordered dolomite structure by Ostwald's rule [13] during early burial time [14, 15], which has been proved by both laboratory experiments and field observations [15–21]. To date, four kinds of microbial-mediated dolomite formation models, including sulfate reduction [12], anaerobic methane-consuming [22], methanogenic model [19, 23], and aerobic oxidation [24] had been hypothesized for various microenvironmental conditions at the water-sediment interface.

As a special type of sediment, lacustrine dolostones in the form of beds or nodules have been widely discovered in the Phanerozoic black shales, including the Middle Permian lake deposits in the Junggar Basin [19], the Later Cretaceous lake deposits in the Songliao Basin [25], and the Early Paleogene lake deposits in the Bohai Bay Basin [26]. These dolomites were supposed to be results of organic matter degradation through biotic and/or abiotic processes during the deposition of organic-rich black shales [19, 25], whereas the causes that triggered the intermittent dolomitization during lacustrine anoxic events remained unknown.

Although much trial has been done in interpreting the genesis of lacustrine dolomite, little emphasis has been put on examining the diagenetic water redox condition(s) during dolomitization. Among all the approaches addressing dolomite formation, X-ray diffraction (XRD) has been mainly adopted for crystal structure analysis [15, 27, 28]. Microscopes, such as scanning electron microscope (SEM) and Cathodoluminescence Microscope (CLM), are also frequently used to observe the dolomite nanocrystals at micro- to nanometer scales [2, 29–31]. However, based on these applications merely, the wealthy geochemical information preserved in primary dolomite, which is believed to archive the aqueous environment as well as biotic and/or abiotic effects during formation, cannot be well characterized. And the sedimentary characteristics documenting the chemical reactions and diagenetic processes would then be ignored. Micro-X-ray fluorescence (μ -XRF) outperforms in achieving the goal mentioned above, which is now thriving in the geological field and has a capability to extract wealthy information from various sediments [32–35]. *In situ* μ -XRF scanning outperforms with its nondestructive, fast, and easy measurement of element spatial distribution with high resolution [36]. And it has been demonstrated to be a powerful tool in understanding the superposition of geological events recorded within modern deltaic, lacustrine, and marine

deposits [36–39], as well as core rocks from ancient geological time [40]. These results radically improve our understanding of paleoclimate and environmental changes, even issues concerning the evolution of the earth system down to annual and even subannual scales. So far, *in situ* μ -XRF scanning has seldom been applied to interpret the genesis of dolomitization, whereas this technique manages to visualize the elemental distribution so as to display delicate genetic characteristics.

Herein, a dolomite nodule from the Late Cretaceous Lake deposits was selected to do scanning with micron resolution by using μ -XRF. Basic guidelines particularly on single-point exposure time and spatial resolution for effective acquisition of elemental and stratigraphic information were proposed. The multielement imaging results are used for interpretation of dolomite genesis, from which the varied redox conditions of the paleo-lake-bottom water and the possible reasons are well depicted. This kind of lacustrine dolomite might serve as the key to unveiling the mystery of dolomite genesis from a comprehensive view of sedimentology and geochemistry.

2. Sample and Methods

2.1. Sample Preparation. The dolomite nodule was sampled from one core with a depth of 2553.6 m in the Songliao Basin, northeast of China. The nodule was well preserved and encased by the black shales of the Upper Cretaceous Qingshankou Formation (Figures 1(a)–1(c)). High-precision CA-ID-TIMS zircon U-Pb dating results (91.886 ± 0.11 Ma, 90.974 ± 0.12 Ma) from the ash layers at the lowermost and uppermost of the first member of Qingshankou Formation, respectively [41] constrain the formation time of the dolomite nodule to be 91 million years ago.

On the polished sectional surface, laminar sedimentary features were easy to be identified both along the edge and inside the nodule (Figure 1(d)). The dolomite sample from the convergent part of this nodule (position around point 3 in Figure 1(d)) and the host black shale were crushed into powders with a tungsten carbide grinding disc for X-ray diffraction tests. A standard thin section with a $1\text{ cm} \times 1\text{ cm}$ area covering the transitional zone between nodule and underlying black shale (area A in Figure 1(d)) was prepared. The sample was placed on a glass slide, and the thickness was reduced by polishing with a Rotpol-35 (Struers) to a standard value of $30\text{ }\mu\text{m}$, which was used for optical and scanning electron microscopic (SEM) observation.

2.2. X-Ray Diffraction. The mineralogy of nodule and host shale were determined in the Research Institute of Petroleum Exploration and Development by using X-ray diffraction (Rigaku SmartLab) equipped with a Cu tube and a monochromator. The powders of nodule and host shale were pressed into cakes with a diameter of 1 cm. The working voltage and current of the X-ray generator were 40 kV and 150 mA, respectively. Scan range (2θ) was selected from 2.6 to 45° with an interval of 0.02° .

2.3. Microscopic Observation. The $30\text{ }\mu\text{m}$ thickness slice sample was examined using an optical microscope (Olympus

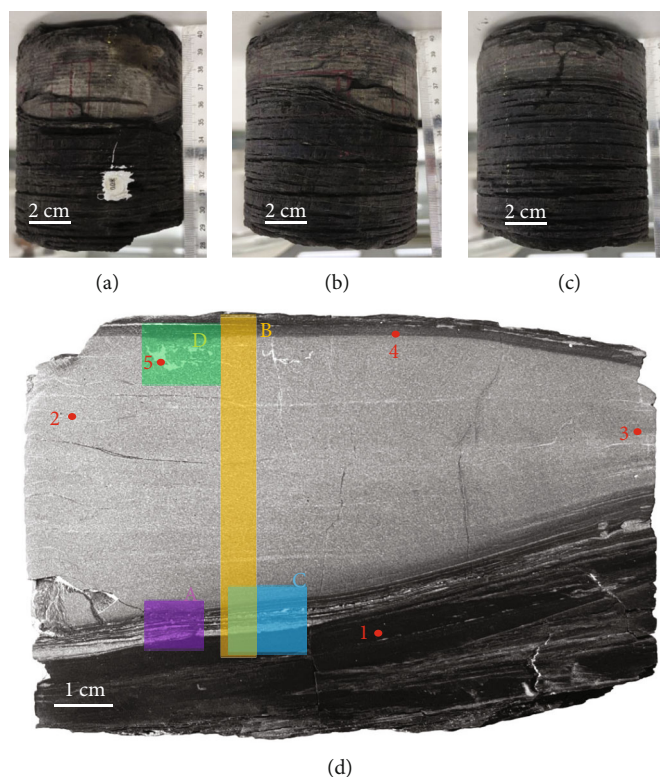


FIGURE 1: Dolomite nodule encased by black shale from front (a), side (b), rear (c), and sectional (d) views. Area A in (d) covering the transitional zone between dolomite nodule and host black shale was observed by using optical microscopy. Five points (1-5) in the sectional surface in (d) were selected to do single-point μ -XRF analysis and parameter optimization. The whole sectional surface and areas B-D were scanned with resolutions of $25\ \mu\text{m}$ and $10\ \mu\text{m}$, respectively, by using μ -XRF.

4500P) to take microphotographs under transmission light. Then, the nodule sample on a glass slide was coated with carbon for scanning electron microscope-energy dispersive X-ray spectroscopy (SEM-EDS) analysis, which was performed using a FEI Apreo equipped with an integrated high-speed detector (Bruker, Germany). The beam accelerating voltage of second electron (SE) images and EDS analyses was 5 kV and 20 kV, respectively. The spot size and working distance were both $5\ \mu\text{m}$. Areas including the core and rim parts within the dolomite nodule were chosen for SEM imaging.

2.4. In Situ μ -XRF Scanning and Multielement Imaging. Multielement in situ X-ray fluorescence (XRF) imaging was performed with a Bruker M4 Tornado Micro-XRF in the Research Institute of Petroleum Exploration and Development. The selected areas were scanned with a $20\ \mu\text{m}$ diameter X-ray beam, which was derived from an Rh anode with a working voltage of 50 kV and a working current of $200\ \mu\text{A}$ at 20 Mbar atmospheric pressure. In a vacuum state, the energy spectrum emitted by the Rh-tube is primarily suitable for the elemental measurements from Na to U. The information of 14 elements (Mg, Al, Si, P, S, K, Ca, V, Cr, Mn, Fe, Sr, Mo, and U) related to the lithological components of dolostone and host shale (e.g., dolomite, ankerite, quartz, and clay minerals) was extracted and analyzed.

Although in situ μ -XRF scanning can provide rapid acquisition of high-resolution elemental datasets, some

experimental parameters, such as single-point exposure time and spatial resolution, have an important influence on the quality and credibility of the data. Increasing single-point exposure time can provide more precise information but greatly extend the whole analysis time. Higher spatial resolution can offer plentiful information from more sites in a reasonable analysis time, with a sacrifice of single-point exposure time which is related to the data accuracy. Therefore, it is necessary to optimize the performing parameters, including single-point exposure time and spatial resolution of the μ -XRF, to obtain sufficiently accurate imaging data in a reasonable testing time.

2.4.1. Single-Point Exposure Time. Before targeting the ideal position for single-point exposure time testing, 5 representative positions in Figure 1(d) were tested with a default exposure time of 10 s and a default beam-diameter of the beam of $25\ \mu\text{m}$. These positions are located at the host black shale (point 1), the inner part of the nodule (point 2), the convergent part of this nodule (point 3), the transitional zone of the black shale and the nodule (point 4), and at an amorphous fallen inclusion (point 5), respectively. Then, 19 single-point exposure times, including 1 ms, 2 ms, 4 ms, 10 ms, 20 ms, 40 ms, 80 ms, 90 ms, 100 ms, 150 ms, 200 ms, 300 ms, 500 ms, 800 ms, 1 s, 5 s, 10 s, 20 s, and 30 s, were conducted at point 2 with 3 times repeat, respectively.

A 5 mm width and 60 mm height area (area B in Figure 1(d)) passing through the nodule and adjacent host

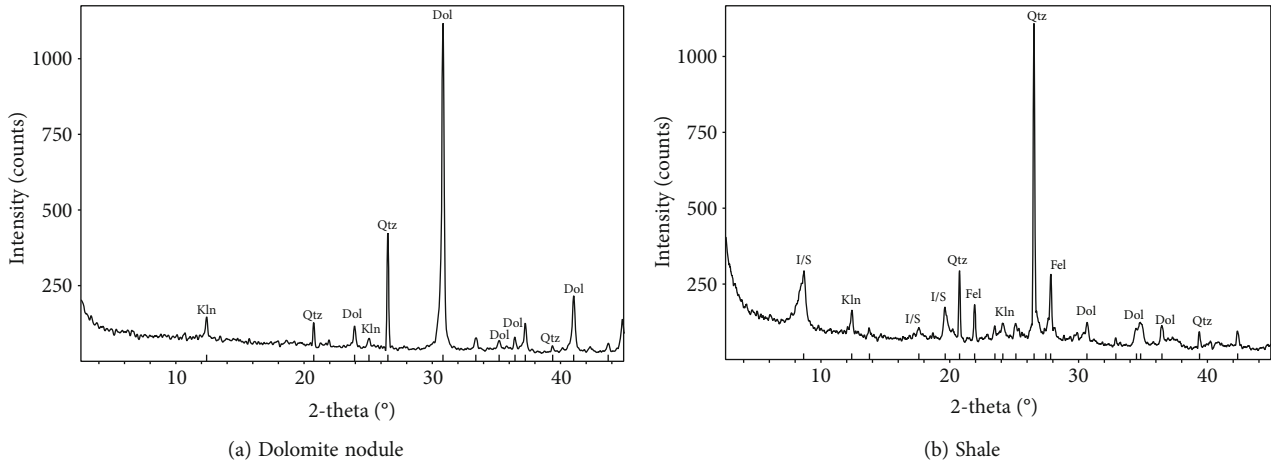


FIGURE 2: X-ray diffraction (XRD) spectra of the dolomite nodule and host black shale. Kln: kaolinite; Qtz: quartz; Dol: dolomite; I/S: illite/smectite; Fel: feldspar.

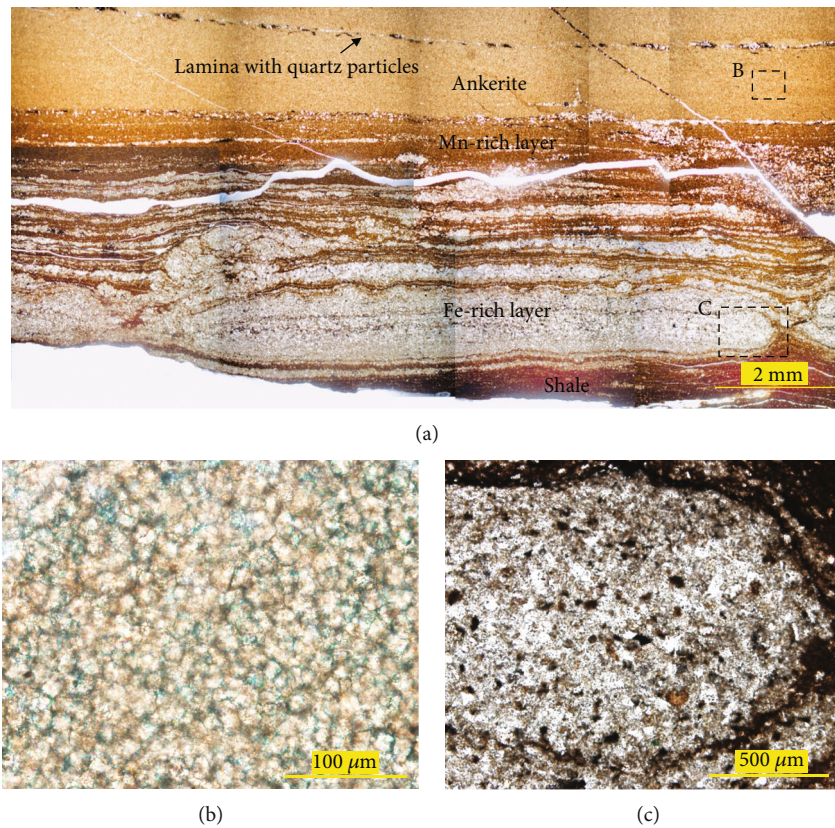


FIGURE 3: (a) Optical pictures of the transient zone from black shale to dolomite nodule, which was taken from area A in Figure 1(d) with microscopic transmission light. The ruler is 2 mm. The lamina pointed with an arrow is a detrital mineral layer containing quartz particles. (b) Amplified image of the dolomite crystals with blue color at their outer rims after dyed with alizarin red, which was a sign of ankerite. The ruler is 100 μm . (c) Amplified image of the convergent part of a quartz debris lens in the host black shale. The ruler is 500 μm .

black shale was selected and scanned with a spatial resolution of 50 μm but different single-point exposure times of 4 ms and 300 ms, respectively.

2.4.2. Spatial Resolution. When the scanned mapping of area B in Figure 1(d) was converted into data, five data moving average types, including 1-point, 2-point, 4-point, 10-point,

and 20-point that corresponded with the spatial resolutions of 50 μm , 100 μm , 200 μm , 500 μm , and 1000 μm , respectively, were chosen to check the minimum requirement of spatial resolution for sedimentary elemental responses.

Considering the elemental responses under different single-point exposure times and spatial resolution requirements, the whole sectional surface was scanned twice with

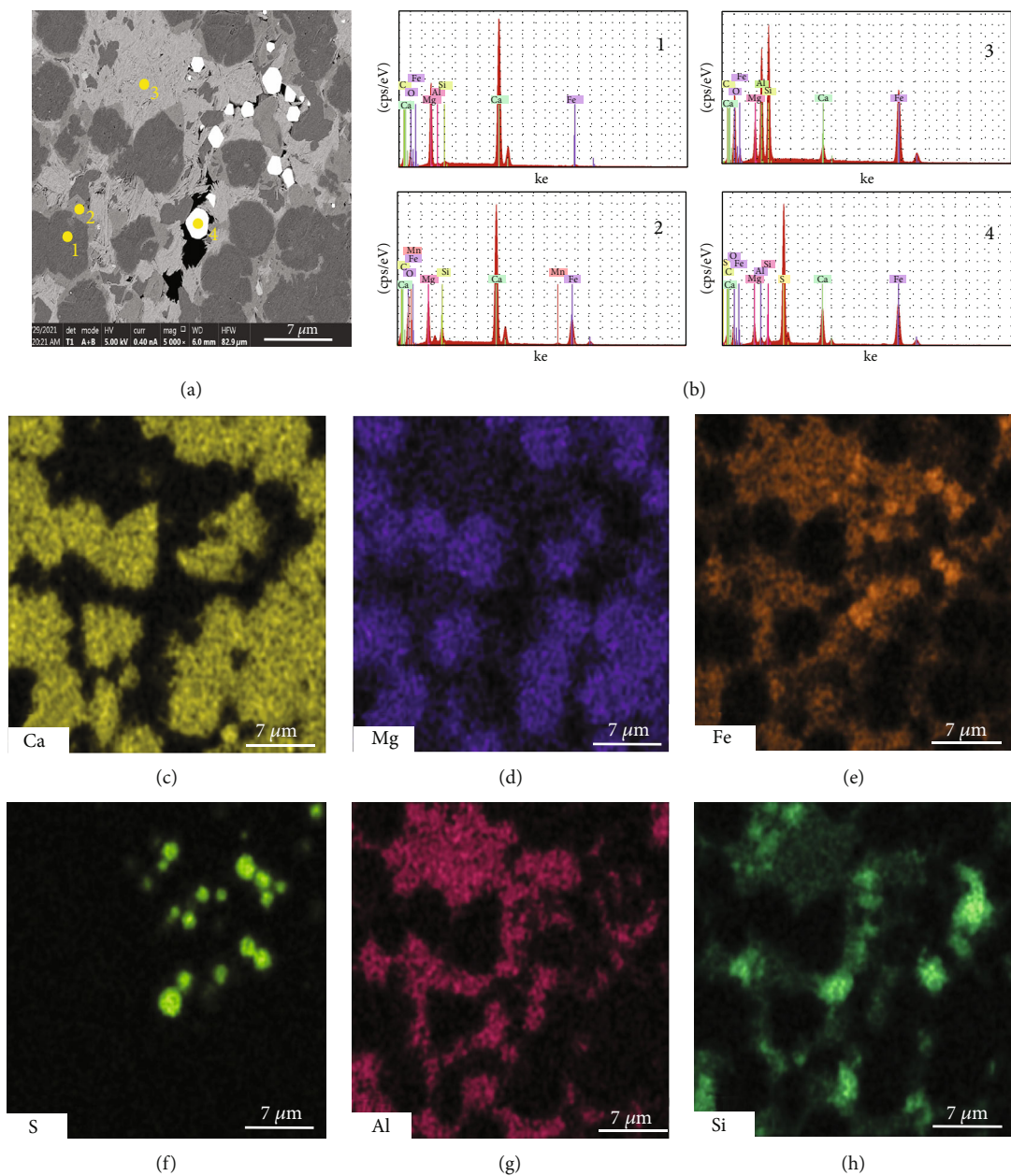


FIGURE 4: SEM image (a) and the corresponding EDX elemental mappings (c–h) of the rim part in dolomite nodule. The EDX spectra of points 1–4 in (a) are shown in (b), which indicate dolomite (1), ankerite (2), chlorite (3), and pyrite (4), respectively.

different parameter settings. The spatial resolution was set as 25 μm vs. 200 μm, while the single-point exposure time was set as 4 ms vs. 300 ms, respectively. The boundary between dolomite nodule and host black shale (area C in Figure 1(d)) and a “drop-stone” (area D in Figure 1(d)) were further scanned with a spatial resolution of 10 μm and a single-point exposure time of 4 ms.

2.5. Statistical Data Processing. The raw elemental data of area B in Figure 1(d) were further investigated by using a principal component analysis (PCA) method to reveal the correlations among elements. The PCA was performed by using the statistical software of SPSS 21, which was capable of simplifying large datasets into several groups of variables

(i.e., factors), with the notion that interrelated results can be categorized into fewer latent variables but do share an unobservable variance. Before extracting factors, tests including Kaiser-Meyer-Olkin (KMO) Measurement of Sampling Adequacy and Bartlett’s Test of Sphericity were conducted to assess the suitability of the PCA method.

3. Results

3.1. Mineral Compositions and Microstructural Characteristics. XRD results show that the nodule is mainly dolomite (70.2%), with small amounts of quartz (14.0%) and clay minerals (15.8%) (Figure 2(a)). Differently, the host black shale is mainly composed of clay minerals (54.0%) and

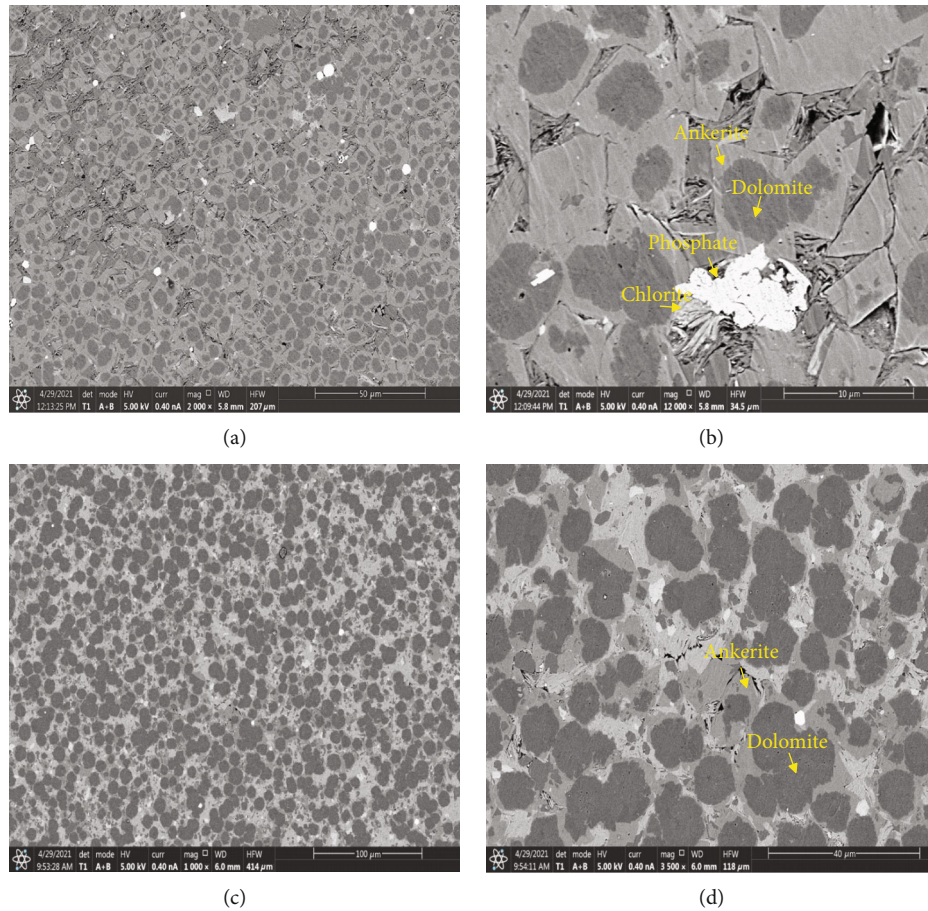


FIGURE 5: SEM images of the core (a, b) and rim (c, d) areas within dolomite nodule. Dolomite crystals in the core area are more ephedra than those in the rim.

quartz (29.1%), with a small proportion of feldspar (12.1%) and dolomite (4.8%) (Figure 2(b)).

Distinct sedimentary characteristics can be revealed under an optical microscope for both nodule and host black shale (Figure 3(a)). The dolomite nodule has microlithic structures with crystals of euhedral-subhedral shape (Figure 3(b)). The blue-colored crystals in Figure 3(b) are a result of alizarin red dyeing, which is a sign of iron in ankerite. Notably, a sandstone lens with poor-roundness quartz particles and dark-colored minerals can be well observed inside the nodule (shown in Figures 3(a) and 3(c)). The host black shale also has obvious laminated sedimentary features, including the black organic-rich layers and white quartz-dominated detritus (Figure 3(a)).

Under SEM, the dolomite crystals show rhombohedrons of euhedral-subhedral shape with diameters of several to tens of micrometers (Figure 4(a)). The dark nucleus and light rim within a single crystal are demonstrated to be dolomite and ankerite, respectively (points 1 and 2 in Figures 4(a) and 4(b)). Chlorite-dominated clay minerals (point 3 in Figures 4(a) and 4(b)) filled in the spaces between dolomite crystals. Pyritohedron-type pyrite crystals (point 4 in Figures 4(a) and 4(b)) with diameters of 1–4 μm are floating in the clay minerals. The above mineral compositions and distributions are further consolidated by the EDS

mapping analysis (Figures 4(c)–4(h)). Notably, dolomite crystals in the core area are more ephedra than those in the rim part (Figure 5), indicating a higher degree of dolomitization inside the nodule.

3.2. Elemental Responses of the Mineral Compositions in the XRF Spectra. XRF spectra at 5 different positions are shown in Figure 6, and the corresponding atomic weight percentages are listed in Table 1. Among them, peaks of Ca and Fe elements were well-detected in shale and dolostone (points 1–4), while Mg and Mn were nearly undetectable at black shale and limestone inclusion (points 1 and 5). Intensive signals of Si, Al, and K in the host black shale indicate the presence of quartzes and clay minerals (point 1). The normalized elemental weight percentage of Mg varied dramatically among different positions, with a slightly high value in the core area of the nodule (point 2, Figure 6(b)), but low in the outer rim part (point 3, Figure 6(c)) and shell area (point 4, Figure 6(d)). Specifically, Mn is concentrated in the shell of the nodule (point 4, Figure 6(d)). Increasing Fe and decreasing Mg contents from core to rim (Figures 6(b)–6(d), Table 1) indicated a substitution of Fe for Mg. Point 5 exhibits an abnormally high content of Ca (Figure 6(e), Table 1), indicating a possible limestone source. The irregular shape and distinct elemental compositions from the host

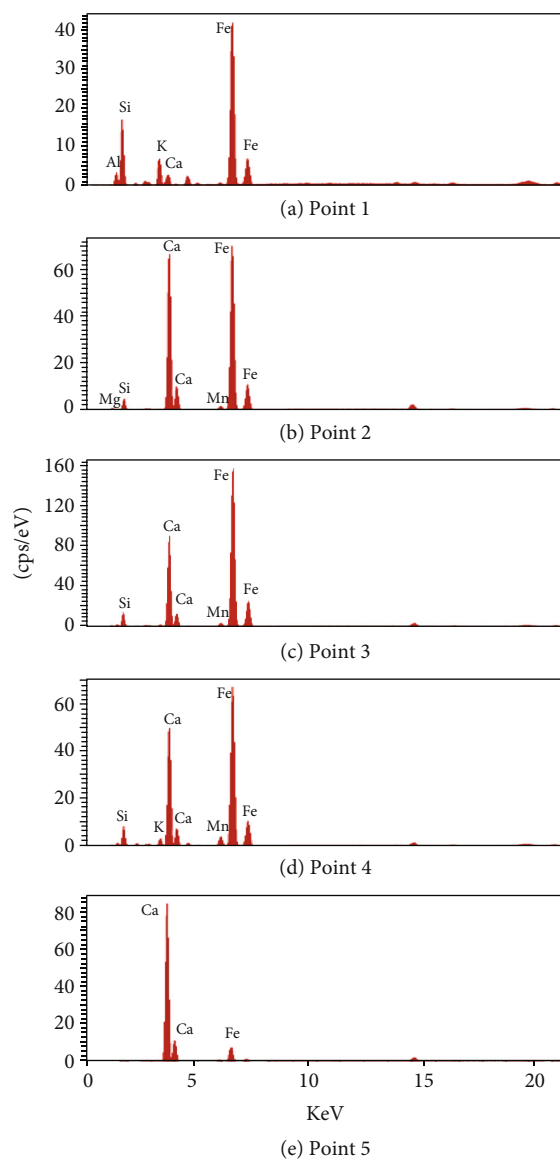


FIGURE 6: Representative XRF spectra of points 1-5 in Figure 1(d) with a $20\ \mu\text{m}$ diameter X-ray beam and a single-point exposure time of 10 s (point 1: black shale; point 2: dolomite; point 3: ankerite; point 4: manganese-ankerite; point 5: limestone inclusion).

dolomite indicated that it might be a “drop-stone” and was enclosed in the dolomite nodule during early diagenesis.

3.3. Parameter Optimization for μ -XRF Measurement

3.3.1. Single-Point Exposure Time. The influences of single-point exposure time on elemental signal intensities were investigated on both single-point measurement and seamless scanning. Point 2 in the core of the nodule (shown in Figure 1(d)) was chosen for single-point measurement.

The normalized elemental weight percentages of Ca, Mg, Fe, and the corresponding data precisions all show significant variations with different exposure times (Figure 7). For all these three elements, 500 ms single-point exposure time is a turning point, from which the accuracy and precision obtained at even longer times exhibited subtle variations. However, the signal responses of Ca, Mg, and Fe

differ a lot at shorter single-point exposure times. Mg tends to be undetectable when exposure time was less than 40 ms (Figure 7), which is attributed to its relatively low-atomic number with extremely small K -fluorescence yield ($\omega_K = 0.022$) [42]. The K -fluorescence yield (ω_K) is the possibility that a K X-ray could be produced once a vacancy is created in the K shell. The values of ω_K for low-atomic-number elements are supremely low (such as Mg), acting as an important factor accounting for their low fluorescence signal intensity. Comparatively, heavier elements, including Ca and Fe in this study, are characterized with much higher K -fluorescence yields ($\omega_{K(\text{Ca})} = 0.164$, $\omega_{K(\text{Fe})} = 0.347$) [43, 44] and thereby easy for detection. However, there is a sharp increase of Ca when exposure time increased from 1 ms to 2 ms, followed by a gradually decreasing trend until 500 ms (Figure 7, Table 2). For both Ca and Fe, shorter exposure time (less than 500 ms) leads to higher but oscillations with large

TABLE 1: Normalized atomic weight percentages of points 1-5 in Figure 1(d). The total percentages lower than 100% were due to the removal of other elements. Slashes of some elements mean their contents are below the detection limits.

Elements	Point 1		Point 2		Point 3		Point 4		Point 5	
	Black shale		Dolomite		Ankerite		Manganese-ankerite		Limestone	
	Ave (%)	std	Ave (%)	std	Ave (%)	std	Ave (%)	std	Ave (%)	std
Mg	0.71	0.14	11.41	0.33	6.73	0.55	3.07	1.39	0.78	0.17
Al	8.34	0.14	1.44	0.12	3.58	0.72	4.82	0.66	0.17	0.08
Si	22.22	0.1	8.84	0.75	12.67	0.1	16.88	3.83	0.61	0.14
P	/	/	0.01	0.02	0.01	0.02	/	/	0.06	0.07
S	0.46	0.05	0.13	0.09	0.09	0.13	0.41	0.33	0.03	0.05
K	2.36	0.19	0.18	0.06	0.17	0.12	1.3	0.11	0.1	0.02
Ca	0.55	0.05	17.61	0.25	11.58	0.12	8.83	3.46	44.49	0.59
Mn	0.02	/	0.18	0.09	0.14	0.02	0.21	0.08	0.27	0.01
Fe	1.49	0.02	4.78	0.11	6.13	0.6	3.54	0.89	2.2	0.29
Sr	0.01	/	0.19	0.15	0.07	0	0.03	0.01	0.24	0.03
Total	36.17	0.07	44.77	0.07	41.17	0.23	39.1	1.52	48.96	0.09

Ave: average; std: standard deviation.

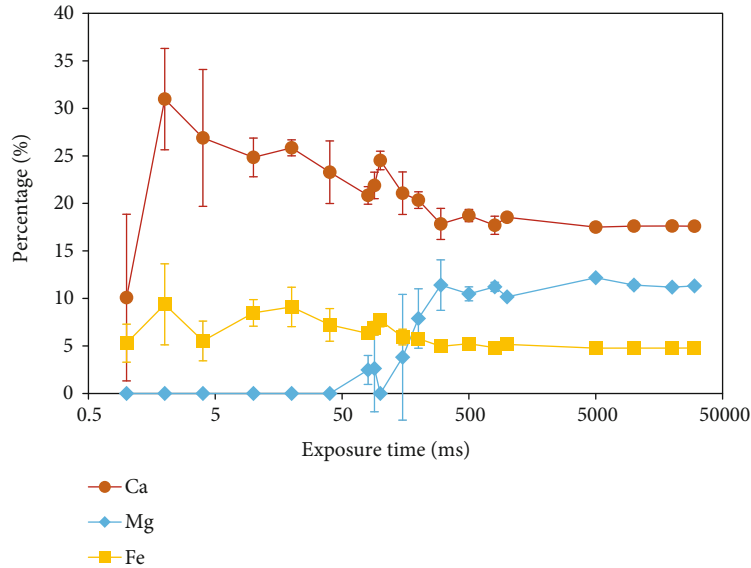


FIGURE 7: Variations of relative atomic percentages of Ca, Mg, and Fe along with logarithm exposure time at point 2 in Figure 1(d).

relative standard deviations (RSDs) (Figure 7, Table 2), which can be used to reflect data precision. Then, an exposure time of no less than 10 s is highly recommended for doing single-point XRF analysis on dolomite samples. This will guarantee the detection of Mg, Ca, Fe, and other major elements with a high level of accuracy (between 97% and 103%) and relative standard deviation (less than 3%) (Table 2).

Long single-point exposure time will definitely prolong the scanning time. To examine whether the extremely short single-point exposure time could achieve multi-element imaging while satisfying the semiquantitative analysis, we compared the scanning results with 4 ms and 300 ms single-point exposure times at the same region (Figure 8). Notably, at a spatial resolution of $50\ \mu\text{m}$, the imaging results for almost all elements with 300 ms single-point exposure time (Figure 8(a)) outperform those

with 4 ms (Figure 8(b)). It is worth noting that, although the signal intensity of Mg in single-point measurement is significantly influenced by the exposure time (Figure 7, Table 2), the exposure time no longer limited Mg detection when doing seamless scanning. Despite a poor resolution, the seamless scanning with a single-point exposure time of 4 ms is still qualified in imaging the distribution of Mg (Figure 8(b)). The enriched and depleted areas of Mg are consistent with the results of 300 ms (Figure 8(a)). Similar great improvements had also been recorded upon P, Sr, Mn, Al, K, and redox-sensitive elements of V, Cr, Mo, and U, but not for Ca, Fe, and Si (Figure 8). A speculation for these results is that the detector could continuously receive XRF signals returned from the sample surface during seamless scanning, and the signal intensities are possibly homogenized.

TABLE 2: Accuracies and relative standard deviations (RSDs) of the measurements of Ca, Mg, and Fe at different exposure times. Data shaded are averaged and presumed as the true values of Ca, Mg, and Fe contents. The RSD data were the same as those in Figure 6. Slashes of Mg mean no signal was detected with the set exposure time.

Exposure time (ms)	Ca		Mg		Fe	
	Accuracies	RSDs	Accuracies	RSDs	Accuracies	RSDs
1	80.65	86.88	/	/	108.04	37.71
2	140.01	17.22	/	/	191.07	45.48
4	192.97	26.77	/	/	112.70	37.90
10	149.73	8.21	/	/	172.88	16.44
20	148.97	3.26	/	/	185.67	22.80
40	115.16	14.13	/	/	147.15	23.75
80	122.38	4.43	22.25	61.44	128.80	5.30
90	115.05	6.38	23.63	173.21	139.89	10.45
100	142.35	3.99	/	/	156.58	8.73
150	103.94	10.60	34.27	173.21	121.04	14.00
200	116.44	4.29	70.82	39.57	117.86	10.61
300	96.48	9.17	102.35	23.26	101.09	10.51
500	105.44	3.44	94.10	7.01	106.74	3.71
800	105.04	5.40	100.74	4.29	98.33	8.66
1000	100.71	2.41	91.29	1.09	105.36	2.69
5000	96.82	0.84	109.35	0.90	97.31	1.10
10000	99.49	1.41	102.41	2.89	97.33	2.26
20000	99.59	1.11	100.48	1.56	97.42	1.86
30000	99.40	0.99	101.65	1.68	97.51	1.19

Note: the accuracy of each element with different single-point exposure times is calculated following these steps. Take Ca as an example, we firstly calculated the average data of normalized atomic weight percentages, as shown in formula (1): $I = (N_{500} + N_{800} + N_{1000} + N_{5000} + N_{10000} + N_{20000} + N_{30000})/7$, where I was the calculated average data, which was also set as the true data. N_i ($i = 500, 800, 1000, 5000, 10000, 20000, 30000$) was the raw normalized atomic weight percentage with a single-point exposure time of 500 ms, 800 ms, 1000 ms, 5000 ms, 10000 ms, 20000 ms, and 30000 ms, respectively. Then, the accuracy of normalized atomic weight percentage with each single-point exposure time was calculated following formula (2): $A = N_i/I \times 100$, where N_i ($i = 1, 2, 4, \dots$) was the raw normalized atomic weight percentage with a single-point exposure time of 1 ms, 2 ms, 4 ms, and so on; A was the accuracy of the raw normalized atomic weight percentage with a single-point exposure time; and I was the calculated average data in formula (1).

3.3.2. Spatial Resolution. Compared with the effect of single-point exposure time, the influence of spatial resolution is far less significant (Figure 9). The elemental profiles with 50 μm and 100 μm spatial resolutions show weak fluctuation, and distortion-free representation of fine-scale structures could be achieved with the resolution of 200 or 500 μm . However, some detailed stratigraphic information was missed in the profile with a resolution of 1000 μm . Seven primary sedimentary cyclicities can be identified according to the records of Ca, Mg, Sr, Fe, Si, and Al (Figure 9). Within each primary cyclicity, secondary sedimentary cyclicities can further be recognized, especially from the variation patterns of Ca, Mg, Sr, and Fe (Figure 9). However, such secondary cyclicity can only be identified with high resolution, saying no less than 500 μm based on our scanning results here.

3.4. Multielement Imaging of the Dolomite Nodule and Host Black Shale

3.4.1. Sectional Scanning in Bulk. According to a previous trial in optimizing single-point exposure time and spatial resolution when doing large-area seamless scanning, the image quality impaired by insufficient single-point exposure time for some elements (e.g., Mg) can be compensated by

continuous signal acquisition. In contrast, the limited image resolution could not be improved by simply increasing exposure time. Therefore, more emphasis should be put on spatial resolution when doing elemental scanning.

The multielement imaging of dolomite nodule and host shale with a spatial resolution of 25 μm and a single-point exposure time of 4 ms is shown in Figure 10. Compared with the host shale, the dolomite nodule is supremely enriched in Ca, P, Mg, Sr, Fe, and Mn, whereas depleted in redox-sensitive (V, Cr, Mo, and U) and terrestrial (Al, K, Si, and S) elements. Interestingly, major elements are not evenly distributed within the nodule. Laminated areas in the core of the nodule are specifically enriched in Ca, P, Mg, and Sr, while Fe is rich in the outer part of the nodule. Mn is intensively concentrated in the “shell” of the nodule, which vanished rapidly both inward and outward, exhibiting a circle-layered pattern. High consistency on the enrichment of Ca and P has been confirmed, and so do Mg and Sr, except for the upper area with an inclusion enclosed. It is noteworthy that some laminae inside the nodule are enriched in Si and S but depleted in Fe; however, the elemental responses of clay minerals shown as Al and K are extremely depleted in the whole nodule. In host black shale, the elemental distributions of Si, S, Al, K, and redox-

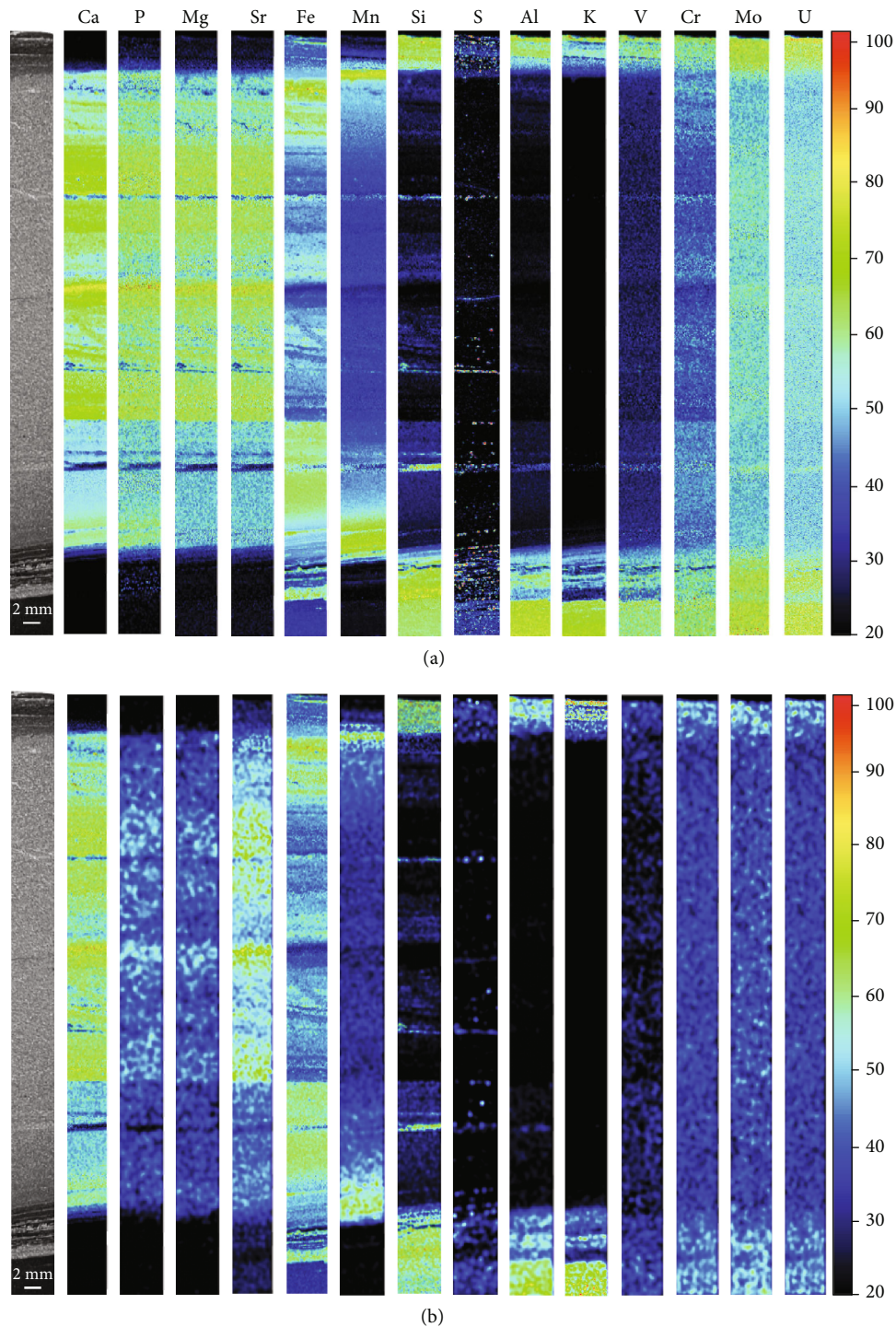


FIGURE 8: Multielement imaging of area B in Figure 1(d) with a single-point exposure time of 300 ms (a) and 4 ms (b), respectively. All images share the same color bar.

sensitive elements (V, Mo, Cr, and U) show obvious consistency. However, Fe and S are decoupled in some areas, as S is depleted in Fe concentrated laminae.

In general, the elemental distributions from the second scanning with a spatial resolution of $200\ \mu\text{m}$ and a single-point exposure time of 300 ms (Figure 11) showed little difference with Figure 10. Longer single-point exposure time does guarantee a better element detection result, but the

differences of elemental enrichments between host shale and nodule did not seem to be significantly improved. This result implies that the loss of elemental signals due to short single-point exposure time could be compensated with more pixels during the seamless scanning. Thus, priority should be given to spatial resolution to capture more geochemical details, rather than exposure time, which prolongs the total measurement time with limited image quality enhancement.

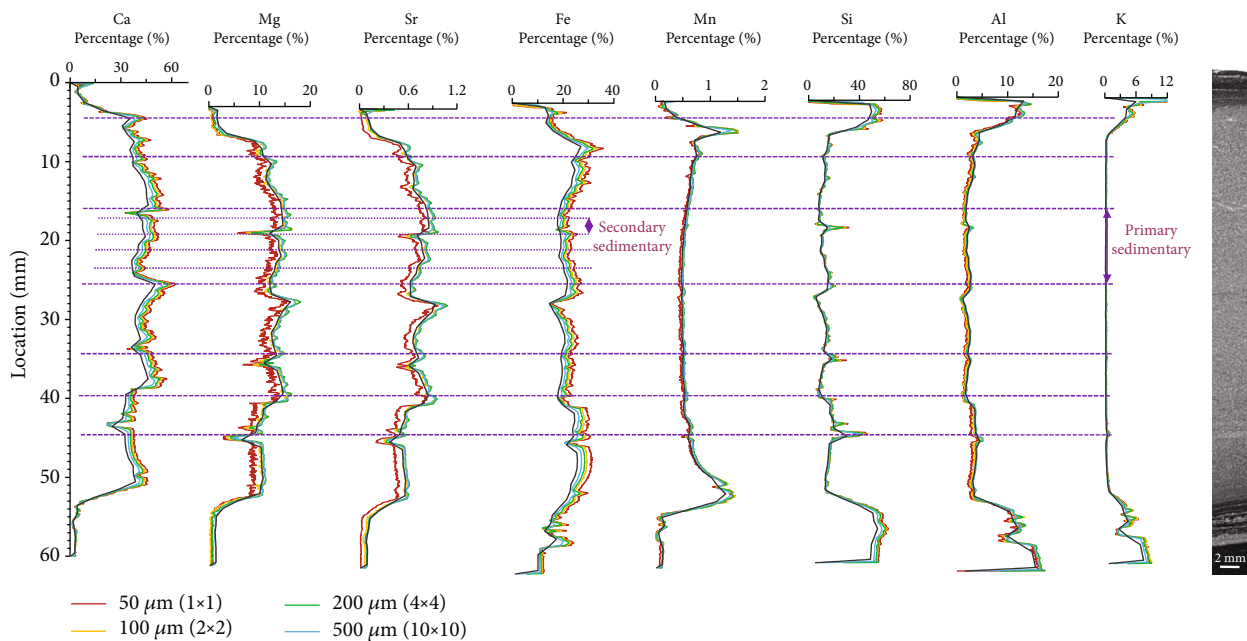


FIGURE 9: Elemental profiles of area B in Figure 1(d) with different resolutions (50 μm , 100 μm , 200 μm , 500 μm , and 1000 μm) after 1 \times 1, 2 \times 2, 4 \times 4, 10 \times 10, and 20 \times 20 points averaged (scanned with 300 ms/pixel). The intervals divided by purple dashed lines represent primary and secondary sedimentary cyclicities with a length of 7.8-9.5 mm and 1-2.5 mm, respectively.

3.4.2. Transitional Zone between Dolomite and Black Shale.

The distinct laminae deposited in the transitional zone between dolomite nodule and black shale may be closely linked with the variations of water environment at early diagenesis. In this view, a delicate scanning of area C in Figure 1(d) was performed with a spatial resolution of 10 μm (Figure 12).

As illustrated in Figure 12, the transitional area from black shale to dolomite nodule contains several layers in the following order: a layer rich in organic matter and clay minerals (shown as the enrichments of Al, K, and redox-sensitive elements), a layer rich in detrital quartz and iron oxide minerals (shown as the enrichments of Si and Fe and depletion of S), another layer rich in organic matter and clay minerals, another layer rich in detrital quartz and iron oxide minerals, and the dolomite nodule finally. Within the nodule, Fe and Mn are enriched alternatively in the shell, while Ca and Mg are more abundant inside the nodule.

3.4.3. Amorphous Fallen Inclusions. It is interesting to dig more information from the amorphous fallen object within area C in Figure 1(d). Scanning with 10 μm spatial resolution clearly outlines these fallen inclusions (Figure 13), which display different sizes with irregular morphologies. The elemental responses of these inclusions differ a lot from the host dolomite, indicating their foreign origin. These inclusions were immobilized in the Fe enrichment zone, which is right under the Mn-rich shell, and are specifically abundant with Ca, P, and Sr (Figure 13). Above the inclusions, Fe is abnormally enriched with slight enrichments of Si and Al, but not for S (Figure 13).

3.5. PCA of Scanning Dataset. Factor analysis outperforms in reducing the dimensionality of a large dataset, so as to simplify the relationships among various elements, which has been widely applied in geological research [45, 46]. The factor loading is a parameter quantifying how much this element contributes to this factor. Here, XRF data of Figure 8(a) with a 1-point moving average was used for statistical assessment. Three factors were extracted and accounted for 86.8% of the variance in the XRF dataset. Based on PCA, four groups are categorized, including elements enriched in dolomite (Ca, P, Mg, and Sr), those entering the dolomite lattice later (Fe, Mn), terrestrial (Si, K, Al, S), and redox-sensitive metal elements (Cr, Mo, V, and U) (Figure 14, Table 3).

4. Discussions

4.1. Genesis of Dolomite Nodule

4.1.1. Dolomite Precursor. The multielemental imaging results here suggested a primary genesis for this lacustrine dolomite nodule. Firstly, the laminated structure inside the nodule, especially the terrestrial detritus deposited inside the nodule (Figure 3), the elemental sedimentary cyclicities (Figure 9), and the initial enrichment of Ca and Mg in dolomite being orchestrated with P and Sr (Figures 10–12), all indicated that the dolomite nodule was originally formed as a laterally connected layer at early diagenesis, which hypothesized its primary genesis. However, with the process of crystallization shrinkage and uninterrupted compaction of overlying sediments, the carbonate rock was pulled up laterally, and thereby forming an ellipsoid shape [47, 48].

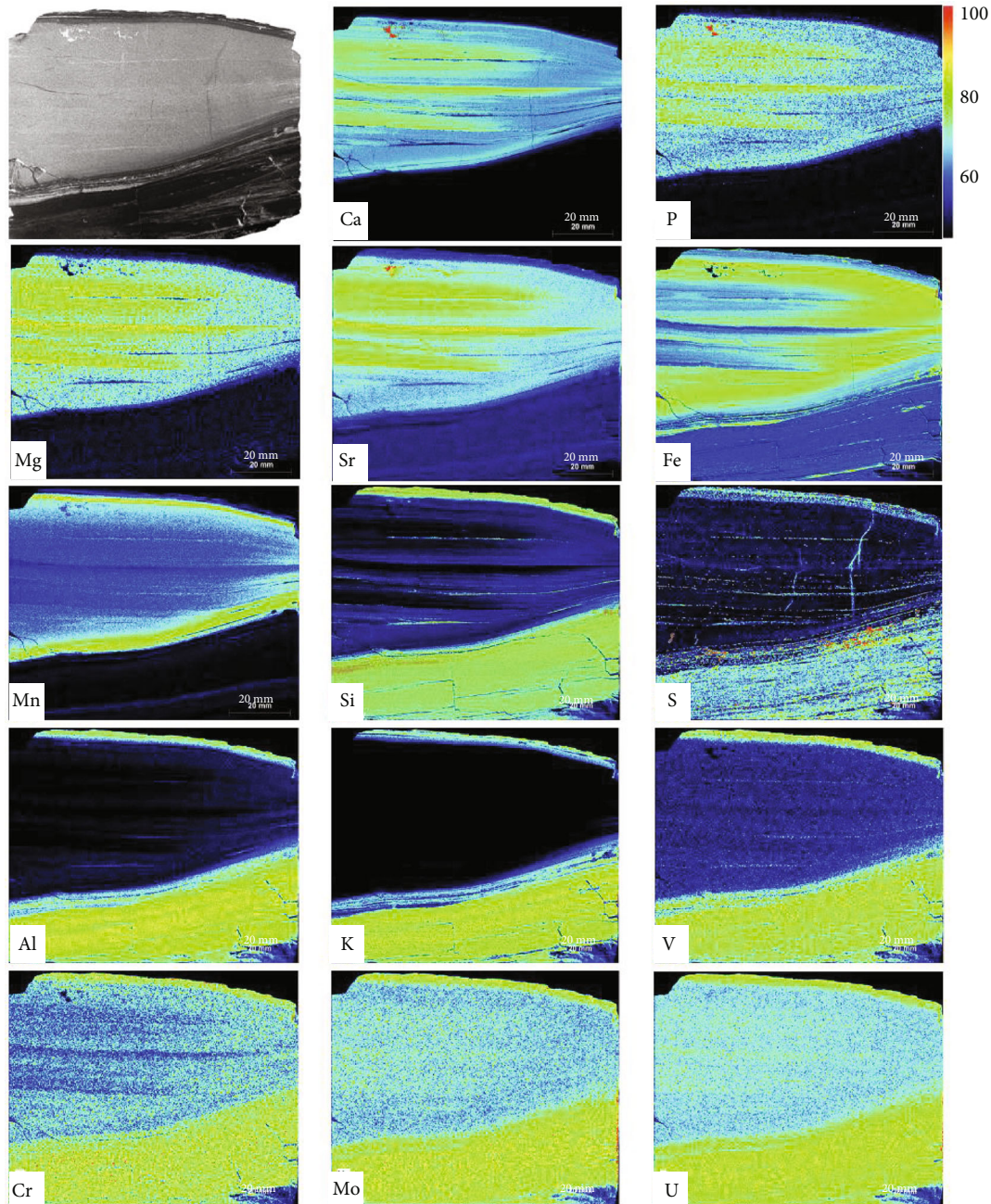


FIGURE 10: Multielement imaging of dolomite nodule and host shale by using XRF. Image size 95.248×73.891 mm (3810×2956 pixels); $25 \mu\text{m}$ pixel size; 4 ms exposure time per pixel. All images share the same color bar.

Secondly, the inclusions in Figure 13 consolidate that the nodule might be plastic colloid at first, rather than rigid. A previous study showed that the organism responsible for Chondrites burrows could transport carbonate cement from a nodule into the surrounding sediment, which would be unlikely unless the nodule was poorly lithified [49]. And the presence of scratch marks on exposed nodules, probably caused by crustaceans, is a particularly persuasive argument in this respect [50]. We thus propose that dolomite was primarily precipitated at early diagenesis at the sediment surface or in the pore water near the water-sediment interface.

Thirdly, the close attachment of dolomite (especially the ankerite crystals) to chlorite flakes in this study is another potent evidence supporting the primary genesis of dolomitization. Highly negative-charged clay minerals manage to catalyze the abiotic precipitation of dolomite at low temperatures [51]. The clay surface could facilitate the process of nucleation, by forming an electrostatic binding with Mg^{2+} and Ca^{2+} ions [52], a possible route for dolomitization in this study.

4.1.2. Penecontemporaneous Replacement of Dolomite into Ankerite. Dolomite could naturally contain minor amounts

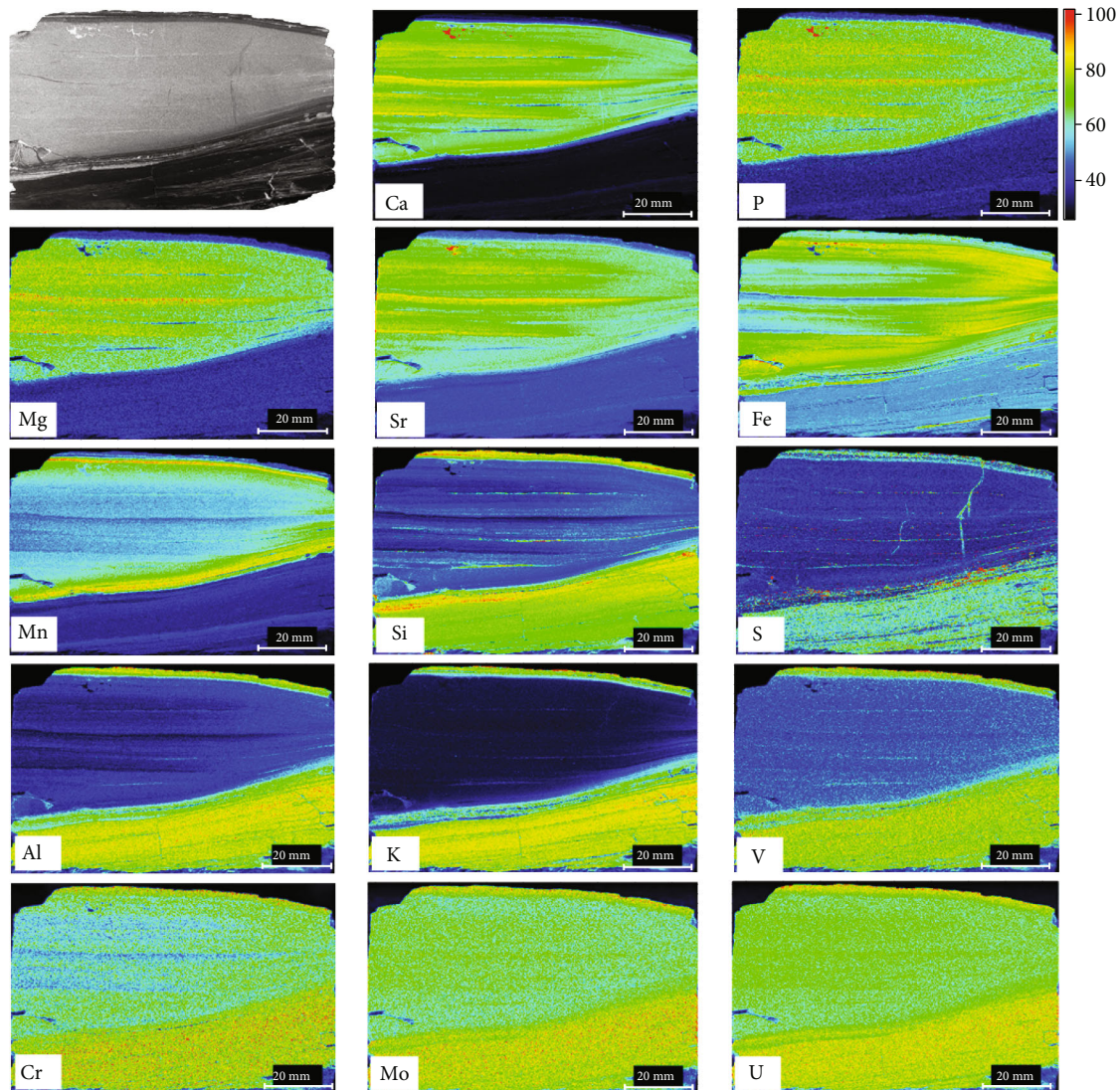


FIGURE 11: XRF elemental maps of dolomite nodule and host shale. Image size 101×76.5 mm (505×382 pixels); $200 \mu\text{m}$ pixel size; 300 ms/pixel. All images share the same color bar.

of element Fe (up to 2 mol%) and trace amounts of Mn (up to several hundreds of ppm) [53]. Because ferrous ion (Fe^{2+}) and magnesium ion (Mg^{2+}) share similar ionic radii, ferrous ions from fluid could easily substitute Mg^{2+} in dolomite and thereby forming ferroan dolomite or ankerite. However, the compositional classification between ferroan dolomite and ankerite is not well defined [3]. Here, the “50% rule” supposed by the International Mineralogical Association guidelines is adopted: any Ca–Mg–Fe carbonate containing less than 50 mol% Fe in the Mg site would be called ferroan dolomite ($\text{Ca}(\text{Fe}_x\text{Mg}_{1-x})(\text{CO}_3)_2$, $0 < x < 0.5$), while more than 50 mol% is called ankerite ($\text{Ca}(\text{Fe}_x\text{Mg}_{1-x})(\text{CO}_3)_2$, $0.5 < x < 1$) [54]. Thus, the relative contents of Fe and Mg at point 2 and point 3 (Figure 1(d), Table 1) consolidate the presence of dolomite and ankerite, respectively.

From core to rim, the increasing trend of Fe and decreasing trend of Mg (Figures 10 and 11) together indicate the penecontemporaneous replacement of Fe-rich fluid at early diagenesis. With the process of crystallization, the inner part

would be impermeable and more closed, while the outer part still has access to the ambient environment. Then, the occasional Fe-rich fluid would lead to ferruginous dolomite at the rim part. And this alternation was supposed to occur at the early diagenetic stage, when pore water was not completely isolated from lacustrine bottom water.

Inside the dolomite nodule, the enrichment of S has been detected in detrital quartz layers, indicating the presence of pyrite. Pyrite crystals have also been recognized in the space between dolomite crystals by using SEM-EDS (Figure 4). As a common sulfide mineral, pyrites distribute widely in argillaceous sediments and usually act as an indicator of sulfate reduction reaction occurring [55]. These pyrites with very fine size (< 4 microns) are generally considered to be formed in euxinic water conditions, indicating a hydrogen sulfide- (H_2S -) containing lake-bottom water with an ephemeral high sulfate reduction rate, during the initial crystallization and cementation stage. The formation of these pyrites is supposed to be mediated by dissimilatory iron-reducing

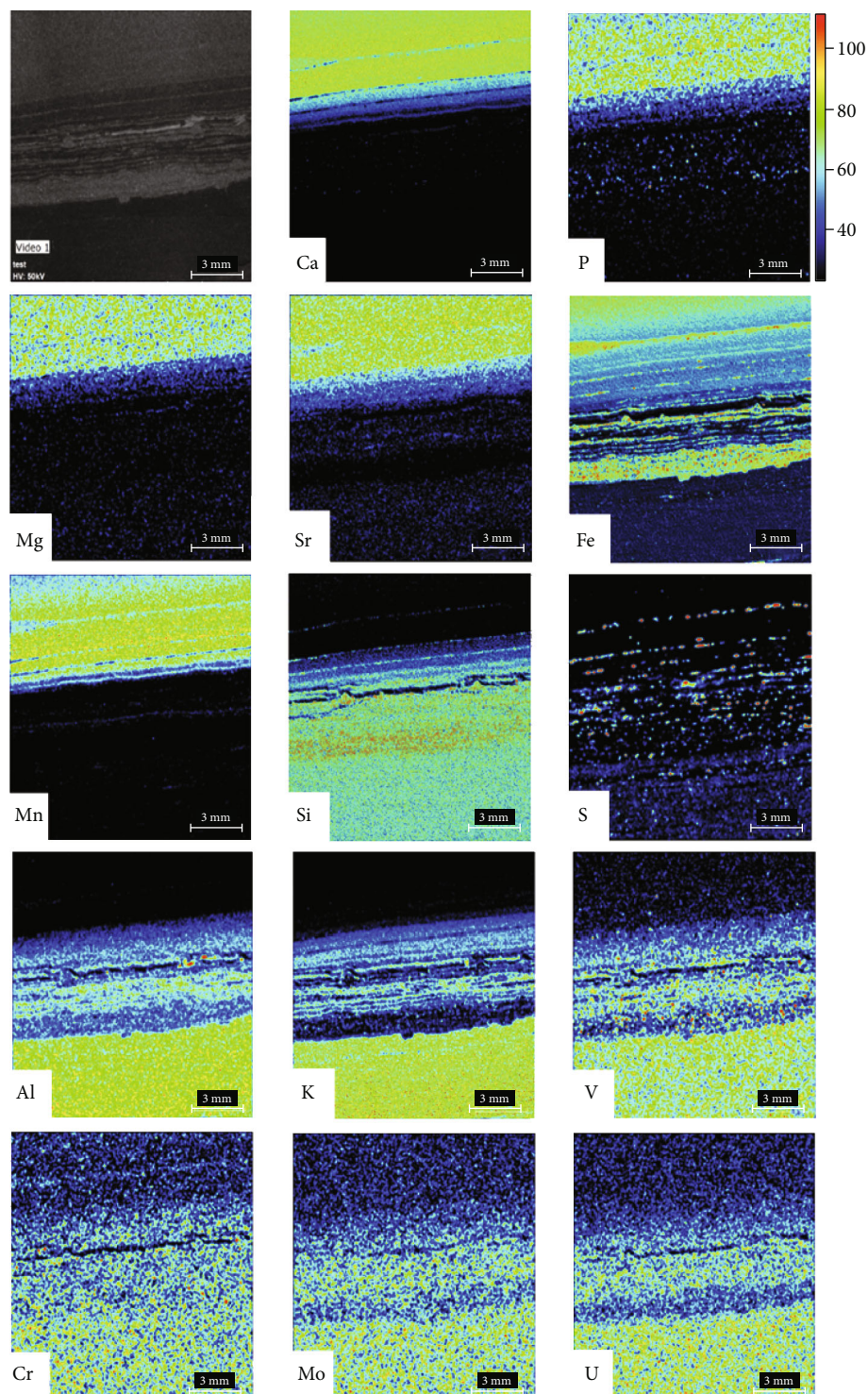


FIGURE 12: Multielement imaging of area C in Figure 1(d) by using XRF. Image size 14×12.9 mm (1400×1290 pixels); $10 \mu\text{m}$ pixel size; 4 ms exposure time per pixel. All images share the same color bar.

bacteria (DIRB) and sulfate-reducing bacteria (SRB) activities [56, 57], which provided Fe^{2+} and H_2S , respectively. Besides, along with the consumption of sulfate by SRB, Mg, which originally existed in strong iron-pairs of Mg^{2+} and SO_4^{2-} , was released into water and further favored the crystallization of dolomite [12]. However, the yield of H_2S might be much lower than that of Fe^{2+} , resulting in a small

amount of pyrite and the mismatches of Fe and S. The excessive Fe^{2+} further entered dolomite lattice to replace Mg^{2+} , causing the initial crystallized dolomite to be converted into ankerite crystals.

4.2. Variations of the Diagenetic Water Redox Conditions. According to the chemical characteristics of redox-active

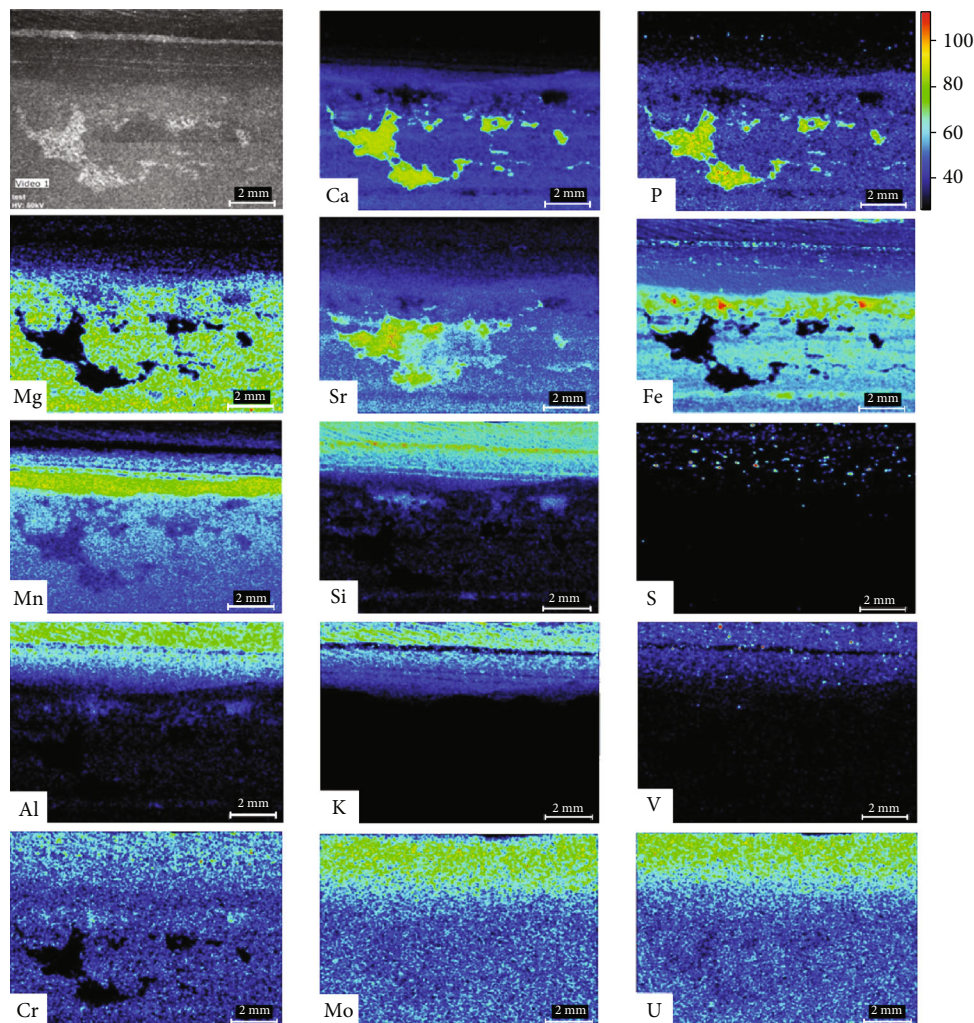


FIGURE 13: Multielement imaging of area D in Figure 1(d) by using XRF. Image size 11.9×9.77 mm (1190×977 pixels); $10 \mu\text{m}$ pixel size; 4 ms exposure time per pixel. All images share the same color bar.

anions and cations (e.g., $\text{NO}_3^-/\text{NO}_2^-$, $\text{Mn}^{4+}/\text{Mn}^{2+}$, $\text{Fe}^{3+}/\text{Fe}^{2+}$, and $\text{SO}_4^{2-}/\text{HS}^-$), the water column can be stratified into different zones [58, 59]. The surface area containing free oxygen to support aerobic metabolisms is referred to be the oxic zone. When oxygen is depleted in a deeper water column, metabolisms contributing to nitrate reduction are called the nitrogenous zone. In or below the nitrogenous zone, dissolved Mn^{2+} typically accumulates as a product of Mn reduction, named as the manganous zone. The removal of dissolved Mn^{2+} deep in anoxic environment is governed, mostly, by carbonate saturation and precipitation [58]. In the deeper ferruginous zone, dissolved Fe^{2+} accumulates due to both biotic and/or abiotic iron oxide reduction. Then, sulfate reduction typically takes place and produces an accumulation of dissolved sulfide in the sulfidic zone. After sulfate is nearly exhausted, methane is accumulated as the methanic zone.

Specifically, according to the chemosedimentary model proposed for calcite [60], high contents of Mn and Fe in calcite could reflect the redox condition of calcite precipitation. This idea is based on the assumption that Mn and Fe contents are closely related to the initial Mn^{2+} and Fe^{2+} in pore water, which are governed by equilibrium with Mn-

and Fe-bearing minerals in the manganous and ferruginous water conditions [4]. Therefore, it is suggested that the distributions of Mn and Fe in dolomite nodule function as an indicator for the chemical conditions of bottom water. Our multi-imaging data of this lacustrine dolomite nodule provides new evidence for this speculation.

As illustrated in Figure 15, the host organic-rich shale beneath the dolomite nodule was believed to be deposited in an sulfidic zone, where redox-sensitive elements (Cr, Mo, V, and U) and S were synchronously enriched (Figures 10 and 11), while the clastic-rich shale might be deposited in an anoxic but nonsulfidic environment due to the decoupling of Fe and S and the depletions of redox-sensitive elements (Cr, Mo, V, and U) (Figures 10 and 11). However, the anoxic even euxinic bottom water might be influenced by the input of oxidized minerals, such as the insoluble MnO_2 , colloidal Fe-oxide minerals (e.g., FeOOH and $\text{Fe}_2\text{O}_3 \cdot n\text{H}_2\text{O}$), insoluble sulfate minerals (e.g., BaSO_4), and strong iron-pairs of MgSO_4 . These oxidized minerals might be carried by gravity flows or saltwater with free oxygen. High rates of BSR, DIR, and dissimilated manganese reduction (DMR) will degrade the organic matter and yield

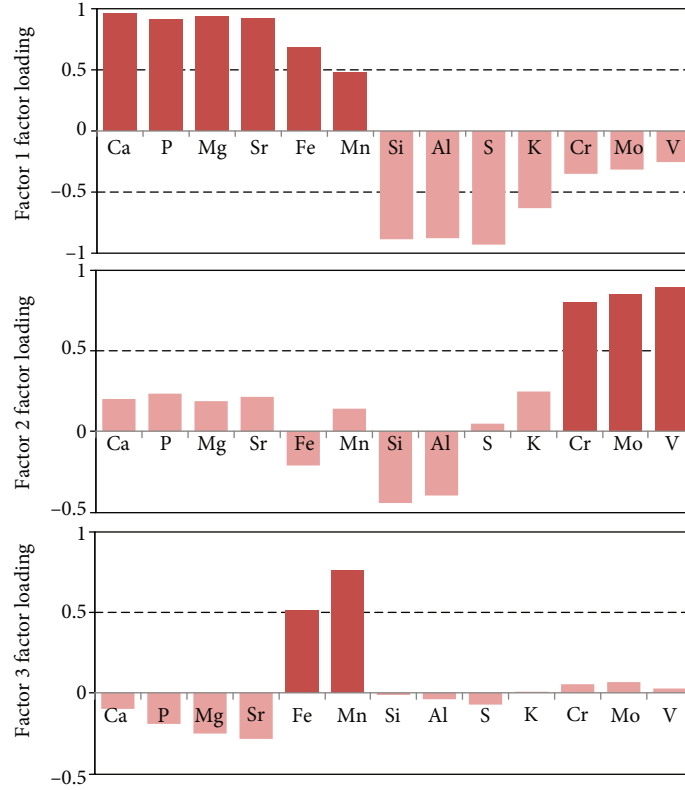


FIGURE 14: Varimax rotated factor loadings extracted by principal component analysis (PCA) on XRF data. The highest factor loadings are dark color-shaded. These three factors account for 86.8% of the total variance, and the extraction rates of all elements are >60%.

TABLE 3: Rotated factor loading matrix by PCA and the categorized element groups.

Elemental category		Element	Factor 1	Factor 2	Factor 3
Elements enriched in dolomite nodule	Originally enriched in dolomite	Ca	0.965	0.213	-0.087
		P	0.921	0.247	-0.177
		Mg	0.944	0.196	-0.241
		Sr	0.926	0.227	-0.269
Elements enriched in dolomite nodule	Later entering dolomite lattice	Fe	0.679	-0.197	0.516
		Mn	0.480	0.152	0.773
Elements enriched in host shale	Terrestrial elements	Si	-0.883	-0.453	-0.017
		Al	-0.876	-0.410	-0.043
		S	-0.937	0.045	-0.072
		K	-0.643	0.148	-0.002
Elements enriched in host shale	Redox-sensitive metal elements	Cr	-0.359	0.786	0.041
		Mo	-0.336	0.844	0.058
		V	-0.279	0.890	0.018
		U	-0.244	0.575	-0.005

Mg^{2+} and HCO_3^- , favoring the formation of dolomite. Then, the excessive Fe^{2+} and Mn^{2+} sequentially lead to ferruginous and manganous zones in the bottom water, which were elaborately recorded in the dolomite nodule. Therefore, the nodule might be formed in a varied water environment with alternative sulfidic and ferruginous conditions, and the dolo-

mitization might come to an end at the manganous zone due to the limited supply of reactants.

4.3. *Possible Reasons for the Formation of Lacustrine Dolomite Nodule.* Similar lacustrine dolostone has been widely discovered in Upper Cretaceous Nenjiang Formation,

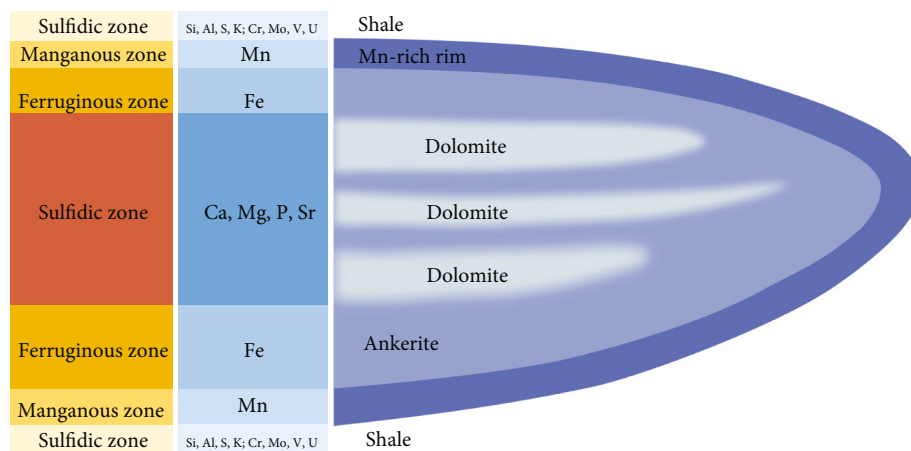


FIGURE 15: Schematic diagram of dolomite nodule embedded in shale with the corresponding enriched elements and redox zones in stratified water column.

Songliao Basin. In the core of CCS-D-SK II, 62 layers of bedded and nodular dolostones were identified in Nenjiang Formation (*ca.* 84 Ma), taking up 2.1% of the total length [48]. Gao et al. suggested naming the dolostone as ferruginous dolomite, a transitional species between dolomite and ankerite in the light of its crystal structure [27]. These dolostones occur as an ellipsoidal lens, of which the interior is characterized with horizontal foliation through the profile. Wang et al. supposed that these dolomites were originated from lacustrine limestone with penecontemporaneous replacement [48]. During the worldwide transgression in Late Cretaceous [61], the large number of ostracoda was extinct and began to deposit due to turbidity disturbance as limestone, which was then dolomitized during the subsequent penecontemporaneous replacement.

However, Liu and Wang [47] assigned the dolomite nodules with internal horizontal laminae to early diagenesis. Together with isotopic compositions of C and Sr, dolomite was thought to be formed in shallow water during the rapid fluctuation of the lake level, which was a result of the mixture of seawater and lake water. Given the presence of pyrite framboids and heavy $\delta^{13}\text{C}$ of dolomite (up to 16‰), Gao et al. asserted that the formation of dolomite was triggered by marine water intrusions, which not only brought Mg^{2+} but also limited the precipitation of carbonate, even leading to fermentation of organic carbon in an anoxic environment [25]. Similar fermentation driven by methanogen was also supposed to have great contributions to the formation of the Permian lacustrine dolomite nodule in the Junggar Basin [19].

Here, we hypothesized that the dolomite nodule in Songliao paleo-lake has a primary genesis with gradual ferruginous and manganous replacements at early diagenesis in the background of periodic seawater intrusions. The originally anaerobic and quiet lacustrine environment was inundated by seawater intrusion, which brought about not only terrestrial debris but also free oxygen, sulfate, and insoluble or colloidal oxidized Fe- and Mn-minerals. Comparatively, Ca and Mg cations might be initially sourced from the lake water, whereas the precipitation was hindered by lacking other essential reactants [62] or the entangling of Mg^{2+} in MgSO_4 ion-pairs [12].

Under seawater intrusion, dolomite crystals were nucleated *via* microbial mediation and then being replaced into ankerite and manganous ankerite at early diagenesis. The sedimentation of dolomite came to an end with the essential reactants being consumed. The bottom water became anoxic even sulfidic again, which favored the preservation of organic matter and black shale deposition.

5. Conclusions

This study demonstrated the superiority of *in situ* μ -XRF in revealing the geochemical information recorded in a lacustrine dolomite nodule from the Songliao Basin in Northeast China, which indicated a primary dolomite precursor being replaced into ankerite at early diagenesis. When optimizing XRF scanning parameters, priority should be given to spatial resolution for more geochemical details, rather than exposure time, which prolongs the total measurement time with limited image quality enhancement. The well-preserved laminated structures inside the nodule and the features with a magnesium-rich core wrapped with an iron-concentric outer layer and a manganese-concentric shell together indicated a primary dolomite precursor and a later penecontemporaneous replacement into ankerite. Multielement imaging graphically revealed the varied diagenetic water redox condition during the formation of the dolomite nodule, which witnessed sulfidic, ferruginous, and manganous zones alternatively. It is hypothesized that the formation of the dolomite nodule was initiated with an abundant supply of sulfate and oxidized Fe-/Mn-rich minerals brought by seawater intrusion, as well as the subsequent microbial mediations, including BSR, DIR, and DMR. Potentially, this dolomite is expected to be a potential fingerprint mineral in tracking the seawater intrusions to the Songliao Basin.

This innovative trial of multielement imaging on the dolomite nodule innovated a new way for the refined research of dolomite by using *in situ* μ -XRF seamless scanning, which is believed to have a great potential in interpreting complicated sedimentological records in both modern and ancient sediments.

Data Availability

All the data referred are shown in the figures and tables in the manuscript file.

Conflicts of Interest

The authors declare that they have no conflicts of interest.

Acknowledgments

The research is financially supported by the Strategic Priority Research Program of the Chinese Academy of Sciences (XDA14010101), the National Natural Science Foundation of China (41872125 and 42002158), the scientific and technological project of RIPED (2021ycq01), and the subject development project of RIPED (yjkt2019-3).

References

- [1] G. D. Dolomieu, "Sur un de pierres tres-peu effervescentes avec les acides of phosphorescentes par la collision," *Journal of Physique*, vol. 39, pp. 3–10, 1791.
- [2] B. Chang, C. Li, D. Liu et al., "Massive formation of early diagenetic dolomite in the Ediacaran Ocean: constraints on the "dolomite problem"," *Proceedings of the National Academy of Sciences of the United States of America*, vol. 117, no. 25, 2020.
- [3] J. M. Gregg, D. L. Bish, S. E. Kaczmarek, and H. G. Machel, "Mineralogy, nucleation and growth of dolomite in the laboratory and sedimentary environment: a review," *Sedimentology*, vol. 62, no. 6, pp. 1749–1769, 2015.
- [4] R. Raiswell and Q. J. Fisher, "Mudrock-hosted carbonate concretions: a review of growth mechanisms and their influence on chemical and isotopic composition," *Journal of the Geological Society*, vol. 157, no. 1, pp. 239–251, 2000.
- [5] Z. Yang, F. F. Whitaker, R. Liu, J. C. Phillips, and D. K. Zhong, "A new model for formation of lacustrine primary dolomite by subaqueous hydrothermal venting," *Geophysical Research Letters*, vol. 48, no. 6, pp. 1–11, 2021.
- [6] H. Li, Y. Liu, K. Yang, Y. Liu, and Y. Niu, "Hydrothermal mineral assemblages of calcite and dolomite–analcime–pyrite in Permian lacustrine Lucaogou mudstones, eastern Junggar Basin," *Northwest China. Mineralogy and Petrology*, vol. 115, no. 1, pp. 63–85, 2021.
- [7] A. Alibrahim, M. J. Duane, and M. Dittrich, "Dolomite genesis in bioturbated marine zones of an early-middle Miocene coastal mud volcano outcrop (Kuwait)," *Scientific Reports*, vol. 11, no. 1, pp. 6636–6654, 2021.
- [8] S. Xiao, C. Zeng, J. Lan et al., "Hydrochemical characteristics and controlling factors of typical dolomite Karst Basin in humid subtropical zone," *Geofluids*, vol. 2021, Article ID 8816097, 14 pages, 2021.
- [9] L. S. Land, "The origin of massive dolomite," *Journal of Geological Education*, vol. 33, no. 2, pp. 112–125, 1985.
- [10] I. Fruth and R. Scherreihs, "Hauptdolomit (Norian) – stratigraphy, paleogeography and diagenesis," *Sedimentary Geology*, vol. 32, no. 3, pp. 195–231, 1982.
- [11] J. Zhang, G. Liu, Z. Cao et al., "Characteristics and formation mechanism of multi-source mixed sedimentary rocks in a saline lake, a case study of the Permian Lucaogou Formation in the Jimusaer Sag, northwest China," *Marine and Petroleum Geology*, vol. 102, pp. 704–724, 2019.
- [12] C. Vasconcelos and J. A. McKenzie, "Microbial mediation of modern dolomite precipitation and diagenesis under anoxic conditions (Lagoa Vermelha, Rio de Janeiro, Brazil)," *Journal of Sedimentary Research*, vol. 67, no. 3, pp. 378–390, 1997.
- [13] S. H. Nordeng and D. F. Sibley, "Dolomite stoichiometry and Ostwald's step rule," *Geochimica et Cosmochimica Acta*, vol. 58, no. 1, pp. 191–196, 1994.
- [14] T. M. Smith and S. L. Dorobek, "Alteration of early-formed dolomite during shallow to deep burial: Mississippian Mission Canyon Formation, central to southwestern Montana," *GSA Bulletin*, vol. 105, no. 11, pp. 1389–1399, 1993.
- [15] A. Bahniuk, J. A. McKenzie, E. Perri et al., "Characterization of environmental conditions during microbial Mg-carbonate precipitation and early diagenetic dolomite crust formation: Brejo do Espinho," *Rio de Janeiro, Brazil. Geological Society London Special Publications*, vol. 418, no. 1, pp. 1010–1015, 2015.
- [16] X. Qiu, H. Wang, Y. Yao, and Y. Duan, "High salinity facilitates dolomite precipitation mediated by *Haloferax volcanii* DS52," *Earth and Planetary Science Letters*, vol. 472, pp. 197–205, 2017.
- [17] G. A. Nadson, "Beitrag zur Kenntniss der bakteriogenen Kalkablagerungen," *Archiv fuer Hydrobiologie*, vol. 19, pp. 154–164, 1928.
- [18] C. Vasconcelos, J. A. McKenzie, S. Bernasconi, D. Grujic, and A. J. Tiens, "Microbial mediation as a possible mechanism for natural dolomite formation at low temperatures," *Nature*, vol. 377, no. 6546, pp. 220–222, 1995.
- [19] F. Sun, W. X. Hu, X. L. Wang et al., "Methanogen microfossils and methanogenesis in Permian lake deposits," *Geology*, vol. 49, no. 1, pp. 13–18, 2021.
- [20] S. Deng, H. Dong, G. Lv, H. Jiang, B. Yu, and M. E. Bishop, "Microbial dolomite precipitation using sulfate reducing and halophilic bacteria: results from Qinghai Lake, Tibetan Plateau, NW China," *Chemical Geology*, vol. 278, no. 3–4, pp. 151–159, 2010.
- [21] D. Liu, N. Yu, D. Papineau et al., "The catalytic role of planktonic aerobic heterotrophic bacteria in protodolomite formation: results from Lake Jibuhulangtu Nuur, Inner Mongolia, China," *Geochimica et Cosmochimica Acta*, vol. 263, pp. 31–49, 2019.
- [22] K. U. Hinrichs, J. M. Hayes, S. P. Sylva, P. G. Brewer, and E. F. Delong, "Methane-consuming archaeobacteria in marine sediments," *Nature*, vol. 398, no. 6730, pp. 802–805, 1999.
- [23] J. A. Roberts, P. C. Bennett, L. A. González, G. L. Macpherson, and K. L. Milliken, "Microbial precipitation of dolomite in methanogenic groundwater," *Geology*, vol. 32, no. 4, pp. 277–280, 2004.
- [24] M. Sánchez-Román, C. Vasconcelos, T. Schmid et al., "Aerobic microbial dolomite at the nanometer scale: implications for the geologic record," *Geology*, vol. 36, no. 11, pp. 879–882, 2008.
- [25] X. Gao, P. Wang, D. Li, Q. Peng, C. Wang, and H. Ma, "Petrologic characteristics and genesis of dolostone from the Campanian of the SK-I Well Core in the Songliao Basin, China," *Geoscience Frontiers*, vol. 3, no. 5, pp. 669–680, 2012.
- [26] Y. Yang, F. H. Gao, X. G. Pu, C. W. Chen, and W. L. Xu, "Changes to depositional palaeoenvironments within the

- Qikou depression (Bohaiwan Basin, China): carbon and oxygen isotopes in lacustrine carbonates of the Palaeogene Shahejie Formation,” *International Geology Review*, vol. 55, no. 15, pp. 1909–1921, 2013.
- [27] X. Gao, P. K. Wang, Q. Y. Li, C. S. Wang, and Y. Gao, “The precise naming and mineralogical characteristics of ferruginous lacustrine dolomite in Well CCSD-SK,” *Acta Petrologica et Mineralogica*, vol. 29, no. 2, pp. 213–218, 2010.
- [28] J. R. Goldsmith, D. L. Graf, and O. I. Joensuu, “The occurrence of magnesian calcites in nature,” *Geochimica et Cosmochimica Acta*, vol. 7, no. 5-6, pp. 212–230, 1955.
- [29] J. D. Kantorowicz, “The origin of authigenic ankerite from the Ninian Field, UK North Sea,” *Nature*, vol. 315, no. 6016, pp. 214–216, 1985.
- [30] H. G. Machel and E. A. Burton, “Factors governing cathodoluminescence in calcite and dolomite, and their implications for studies of carbonate diagenesis,” *SEP Special Publications*, vol. 25, pp. 37–57, 1991.
- [31] Y. Zeng, J. Zhang, and H. Zheng, “The origin of middle and upper Devonian dolomite in the Tangwanzhai area, Longmen Mountains, Sichuan Province,” *Geological Review*, vol. 37, no. 1, pp. 1–12, 1991.
- [32] B. Gregory, R. T. Patterson, E. G. Reinhardt, J. M. Galloway, and H. M. Roe, “An evaluation of methodologies for calibrating Itrax X-ray fluorescence counts with ICP-MS concentration data for discrete sediment samples,” *Chemical Geology*, vol. 521, pp. 12–27, 2019.
- [33] J. A. Richardson, M. Newville, A. Lanzirotti et al., “The source of sulfate in brachiopod calcite: insights from μ -XRF imaging and XANES spectroscopy,” *Chemical Geology*, vol. 529, article 119328, 2019.
- [34] F. Zhang, H. J. Wang, Y. T. Ye et al., “The environmental context of carbonaceous compressions and implications for organism preservation 1.40 Ga and 0.63 Ga,” *Palaeogeography, Palaeoclimatology, Palaeoecology*, vol. 573, article 110449, 2021.
- [35] B. D. Stewart, J. V. Sorensen, K. Wendt et al., “A multi-modal approach to measuring particulate iron speciation in buoyant hydrothermal plumes,” *Chemical Geology*, vol. 560, article 120018, 2021.
- [36] L. Lowemark, H. F. Chen, T. N. Yang et al., “Normalizing XRF-scanner data: a cautionary note on the interpretation of high-resolution records from organic-rich lakes,” *Journal of Asian Earth Sciences*, vol. 40, no. 6, pp. 1250–1256, 2011.
- [37] Y. Kido, T. Koshikawa, and R. Tada, “Rapid and quantitative major element analysis method for wet fine-grained sediments using an XRF microscanner,” *Marine Geology*, vol. 229, no. 3-4, pp. 209–225, 2006.
- [38] R. Hennekam and G. de Lange, “X-ray fluorescence core scanning of wet marine sediments: methods to improve quality and reproducibility of high-resolution paleoenvironmental records,” *Limnology & Oceanography Methods*, vol. 10, no. 12, pp. 991–1003, 2012.
- [39] I. W. Croudace and R. G. Rothwell, “Micro-XRF studies of sediment cores: a perspective on capability and application in the environmental sciences,” in *Micro-XRF studies of sediment cores*, pp. 1–21, Springer, 2015.
- [40] C. Liu, K. Y. Liu, X. Q. Wang, R. K. Zhu, L. Y. Wu, and X. Y. Xu, “Chemo-sedimentary facies analysis of fine-grained sediment formations: an example from the Lucaogou Fm in the Jimusaer sag, Junggar Basin, NW China,” *Marine and Petroleum Geology*, vol. 110, pp. 388–402, 2019.
- [41] T. Wang, J. Ramezani, C. Wang, H. Wu, H. He, and S. A. Bowring, “High-precision U-Pb geochronologic constraints on the Late Cretaceous terrestrial cyclostratigraphy and geomagnetic polarity from the Songliao Basin, Northeast China,” *Earth and Planetary Science Letters*, vol. 446, pp. 37–44, 2016.
- [42] W. Bambynek, B. Crasemann, R. W. Fink et al., “X-ray fluorescence yields, Auger, and Coster-Kronig transition probabilities,” *Reviews of Modern Physics*, vol. 44, no. 4, pp. 716–813, 1972.
- [43] V. A. Sole, B. Denecke, G. Grosse, and W. Bambynek, “Measurement of the K-shell fluorescence yield of Ca and K with a windowless Si(Li) detector,” *Nuclear Instruments and Methods in Physics Research Section A: Accelerators, Spectrometers, Detectors and Associated Equipment*, vol. 329, no. 3, pp. 418–418, 1993.
- [44] L. E. Bailey and J. B. Swedlund, “X-ray fluorescence yields of Al, Cl, Ar, Sc, Ti, V, Mn, Fe, Co, Y, and Ag,” *Physical Review*, vol. 158, no. 1, pp. 6–13, 1967.
- [45] Y. Ye, H. J. Wang, X. M. Wang, L. N. Zhai, C. D. Wu, and S. C. Zhang, “Elemental geochemistry of lower Cambrian phosphate nodules in Guizhou Province, South China: an integrated study by LA-ICP-MS mapping and solution ICP-MS,” *Palaeogeography, Palaeoclimatology, Palaeoecology*, vol. 538, article 109459, 2020.
- [46] Z. A. Berner, H. Puchelt, T. Nöltner, and U. Kramar, “Pyrite geochemistry in the Toarcian Posidonia Shale of south-west Germany: evidence for contrasting trace-element patterns of diagenetic and syngenetic pyrites,” *Sedimentology*, vol. 60, no. 2, pp. 548–573, 2013.
- [47] W. Liu and P. Wang, “Genesis and environmental significance of the dolomite concretions from the Nenjiang Formation in the Songliao Basin, Northeastern China,” *Lithofacies Paleogeography*, vol. 17, no. 1, pp. 22–26, 1997.
- [48] G. Wang, R. H. Cheng, P. J. Wang, and Y. F. Gao, “The forming mechanism of dolostone of Nenjiang Formation in Songliao Basin—example from CCSD-SK II,” *Acta Geologica Sinica*, vol. 82, no. 1, pp. 48–54, 2008.
- [49] K. Bjorlykke, “Origin of limestone nodules in the Lower Paleozoic of the Oslo region,” *Norsk Geologisk Tidsskrift*, vol. 53, pp. 419–431, 1973.
- [50] S. P. Hesselbo and T. J. Palmer, “Reworked early diagenetic concretions and the bioerosional origin of a regional discontinuity within British Jurassic marine mudstones,” *Sedimentology*, vol. 39, no. 6, pp. 1045–1065, 1992.
- [51] Y. Wen, S. R. Mónica, Y. L. Li et al., “Nucleation and stabilization of Eocene dolomite in evaporative lacustrine deposits from central Tibetan plateau,” *Sedimentology*, vol. 67, pp. 3333–3354, 2020.
- [52] D. Liu, Y. Y. Xu, D. Papineau et al., “Experimental evidence for abiotic formation of low-temperature proto-dolomite facilitated by clay minerals,” *Geochimica et Cosmochimica Acta*, vol. 247, pp. 83–95, 2019.
- [53] C. Klein and B. Dutrow, *Manual of Mineral Science*, Wiley, 2010.
- [54] E. H. Nickel and J. D. Grice, “The IMA Commission on New Minerals and Mineral Names: procedures and guidelines on mineral nomenclature, 1998,” *Mineralogy and Petrology*, vol. 64, no. 1-4, pp. 237–263, 1998.
- [55] D. E. Canfield, S. Zhang, H. Wang et al., “A Mesoproterozoic iron formation,” *Proceedings of the National Academy of Sciences*, vol. 116, no. 12, pp. 5800–5805, 2019.

- Sciences of the United States of America*, vol. 115, no. 17, pp. 3895–3904, 2018.
- [56] R. A. Berner, “Sedimentary pyrite formation: an update,” *Geochimica et Cosmochimica Acta*, vol. 48, no. 4, pp. 605–615, 1984.
- [57] J. K. Fredrickson, H. M. Kostandarithes, S. W. Li, A. E. Plymale, and M. J. Daly, “Reduction of Fe(III), Cr(VI), U(VI), and Tc(VII) by *Deinococcus radiodurans*R1,” *Applied & Environmental Microbiology*, vol. 66, no. 5, pp. 2006–2011, 2000.
- [58] D. E. Canfield and B. Thamdrup, “Towards a consistent classification scheme for geochemical environments, or, why we wish the term ‘suboxic’ would go away,” *Geobiology*, vol. 7, no. 4, pp. 385–392, 2009.
- [59] C. Li, M. Cheng, A. Thomas, and S. C. Xie, “A theoretical prediction of chemical zonation in early oceans (>520 Ma),” *Science*, vol. 11, pp. 1901–1909, 2015.
- [60] R. J. Barnaby and J. D. Rimstidt, “Redox conditions of calcite cementation interpreted from Mn and Fe contents of authigenic calcites,” *Geological Society of America Bulletin*, vol. 101, no. 6, pp. 795–804, 1989.
- [61] P. C. de Graciansky, G. Deroo, J. P. Herbin et al., “Ocean-wide stagnation episode in the late Cretaceous,” *Nature*, vol. 308, no. 5957, pp. 346–349, 1984.
- [62] X. Zhang, “Study on the origin of the dolostone intercalated in the black shales in middle Permian Lucaogou Formation eastern part of southern margin of Junggar Basin,” *Acta Sedimentologica Sinica*, vol. 11, no. 2, pp. 133–140, 1993.